Manuscript Information

Journal name:	Nature photonics
Manuscript #:	64183
Manuscript Title:	Role of microstructure in the electron-hole interaction of hybrid lead-halide perovskites
Principal Investigator:	
Submitter:	Nature Publishing Group (repositorynotifs@nature.com)

Manuscript Files

Type	Fig/Table #	Filename	Size	Uploaded
manuscript	1	NIHMS64183-manuscript.pdf	213569	2015-07-14 11:17:21
figure	1	figure_1.pdf	9104250	2015-07-14 11:03:58
figure	2	figure_2.pdf	11069328	2015-07-14 11:04:01
figure	3	figure_3.pdf	231876	2015-07-14 11:04:02
figure	4	figure_4.png	620329	2015-07-14 11:04:02
supplement	1	supp_info_1.pdf	1567974	2015-07-14 11:04:02

Role of Microstructure in the Electron-Hole Interaction of Hybrid Lead-Halide Perovskites

Giulia Grancini[1‡], Ajay Ram Srimath Kandada[1‡], Jarvist M. Frost[2], Alex J. Barker[1], Michele De Bastiani[1,3], Marina Gandini[1], Sergio Marras[4], Guglielmo Lanzani[1], Aron Walsh[2] and Annamaria Petrozza[1]*

[1] Center for Nano Science and Technology @Polimi, Istituto Italiano di Tecnologia, via Giovanni Pascoli 70/3, 20133, Milan, Italy

[2] Centre for Sustainable Chemical Technologies and Department of Chemistry, University of Bath, Claverton Down, Bath BA2 7AY, United Kingdom

[3] Dipartimento di Scienze Chimiche, Università degli Studi di Padova, via Marzolo 1, 35131 Padova, Italy

[4] Department of Nanochemistry, Istituto Italiano di Tecnologia, via Morego 30, 16163 Genova, Italy

* annamaria.petrozza@iit.it

[‡]These authors equally contributed.

Solar cells based on hybrid inorganic-organic halide perovskites have demonstrated high power conversion efficiencies in a range of architectures. The existence and stability of bound electron-hole pairs in these materials, and their role in the exceptional performance of optoelectronic devices, remains a controversial issue. Here we demonstrate, through a combination of optical

spectroscopy and multiscale modeling as a function of the degree of polycrystallinity and temperature, that the electron-hole interaction is sensitive to the microstructure of the material. The long-range order is disrupted by polycrystalline disorder and the variations in electrostatic potential found for smaller crystals suppress exciton formation, while larger crystals of the same composition demonstrate an unambiguous excitonic state. We conclude that fabrication procedures and morphology strongly influence perovskite behaviour, with both free carrier and excitonic regimes possible, with strong implications for optoelectronic devices.

Hybrid perovskites represent a new, disruptive technology in the field of optoelectronics. They have the potential to overcome the performance limits of current technologies and achieving low cost and high integrability. Hybrid halide perovskite, e.g. $CH_3NH_3PbX_3$ [X = Cl, Br, or I], solar cells with power conversion efficiency exceeding 20% [1, 2] are effectively challenging existing thin-film technologies. In addition, the incorporation of hybrid perovskites in optical cavities as lasing materials [3,4,5] and in diode structures as efficient light emitters[6] demonstrates their flexibility and potential for technologically relevant applications beyond photovoltaics.

Hybrid perovskites are usually deposited as polycrystalline thin-films with variable mesoscale morphology depending on the growth conditions and the obtained grain size ranges from tens to thousands of nm [7–9]. Over the last two years the impressive improvement of photovoltaic performance has been driven by empirical evolution of the

device architecture and processing methodologies. However, there is a considerable lack of understanding of material properties, both as pristine films and their embodiment in a device. Early studies classified the working mechanism of perovskite based-solar cells within a pure excitonic paradigm, [10] with bound electron and hole pairs being the primary photoexcitation. More recent investigations have put forward a different scenario, where photoexcitation leads mainly to the generation of free electrons and holes, similar to the case of conventional polycrystalline inorganic semiconductors[4,11–16]. Recently, there have been several reports on the optical properties of hybrid perovskite single crystals[17–19], which should represent a reliable reference state. However, even in this case, a few discrepancies are evident, for example, Shi et al.[17] report an optical absorption spectrum with onset at 1.63eV, showing no sign of excitonic states[17], while J. Huang et al.[18] show evidence of a strong excitonic peak at the onset of the external quantum efficiency spectrum, at 1.51 eV[18].

In this report we describe the interplay between free carriers and excitons, based on transient absorption (TA) spectroscopy and multi-scale numerical simulations. $CH_3NH_3PbI_3$ ($MAPbI_3$) crystallized in a mesoporous scaffold, with small grain size (tens of nm), does not support exciton states even at low temperature. In contrast, in hundreds of nm-large domains, as formed by the deposition on flat substrate, free carriers may thermalize and coalesce into the *exciton state* – depending on temperature and excitation density. Similar behavior is also observed for the higher band gap $CH_3NH_3PbBr_3$ ($MAPbBr_3$). Thus, a definitive classification – “excitonic” or “free carrier” semiconductor – as well as a universal value for the exciton binding energy in semiconductors presenting the same chemical composition, is not possible for hybrid

perovskites as both regimes are physically accessible by appropriately processing the compounds. We rationalize this by introducing a model for dielectric screening in perovskites. Such a screening is due to polarization of the medium, and can originate from electronic as well as lattice displacements. Here we find it is strongly dependent on the coherent long-range order in the lattice which can be disrupted by imperfections, such as domain walls within crystals or surface defects. As the permanent dipoles associated with the methylammonium cation are free to move within the inorganic cage of the hybrid perovskites, they contribute to lattice polarization, screening the electron-hole Coulomb interaction.

We first consider a $MAPbI_3$ film fabricated by the two-step deposition method on 3 μm thick alumina mesoporous scaffold, as one of the most established architecture for efficient perovskite solar cells[20] (see Experimental methods for the details on sample preparation). This sample provides simultaneous access to two distinct structural morphologies: the crystalline phase grown within the scaffold (meso phase in the following), which, on average, limits the crystal size to the nanometer scale[7,9] and the thick capping layer on top of the scaffold, consisting of crystals up to hundreds of nm in size (see Figures 1a and b, respectively and XRD analysis in Figure S1 in SI). The temperature dependent optical absorption spectrum of such a sample is reported in Figure S2 of the Supplementary Information (SI) and does not show any excitonic transition at its onset, similar to what we have previously reported[12].

In agreement with previous works[4,11,21] the TA spectral evolution of the meso phase upon photoexcitation above the band-edge can be accounted for by considering the photo-induced charge-carrier dynamics, without invoking any excitonic contributions.

Note that the sample was photo-excited from the substrate side in order to selectively interrogate the perovskite phase grown in the scaffold. At room temperature (RT), the bleaching signal around 1.67 eV shows a rise with time constant of 260 fs due to the hot-carrier thermalization to the band edge and a broad photo-induced absorption (PA_1) band that forms for energies higher than 1.77 eV. Briefly, the PB band is assigned to the band filling of the free carriers, while the PA_1 has been tentatively assigned in literature to the change in the refractive index induced by the free carrier population[4,11,21] (see Figures S3 and S4 and the detailed discussion in the SI). In Figure 1c, by reducing the temperature, still above the tetragonal-to-orthorhombic phase transition, we observe that the PB band red-shifts, gets narrower and gains intensity. The change in the line shape is consistent with the lower thermal energy that reduces the homogeneous broadening. The red shift can be simply related to the Varshni effect [22](see discussion in Figure S5 in the SI). It is worth underlining here that this sample *does not show* any excitonic peak in the absorption spectrum even at 4K (see Figure S2b).

In Figure 1d we show the temperature dependent TA spectra of the *same* sample illuminated from the capping side. Since pump photon penetration depth is comparable to the thickness of the capping layer, we mainly excite the large crystals in the capping phase, [40] though some contribution from the smaller crystals within the scaffold can be present (see Figure 1b). At RT we note that the PB band is broader and red-shifted with respect to the PB of the meso phase of the film. The red shift is due to the reduction of the band gap in the large crystals,[13] while the broadening can be related to contributions from the meso phase underneath. The most striking difference appears when the sample is cooled down. In particular, at 170K the PB band is strongly red-

shifted. Such a large red-shift does not follow the standard Varshni trend. Furthermore, the PA_1 band is simultaneously quenched and a new negative band appears, peaking around 1.67eV. Note that this is not simply related to the low-temperature structural phase transition that occurs below 170K [12,23] *,* which would lead to a blue shift of the whole spectrum as a consequence of a widening of the semiconductor band-gap (see Figures S6 and S7 and the discussion in SI). The time evolution of the TA spectra at 170K is shown in Figure 1e. At 200 fs a positive band peaking close to 1.63 eV is present. In about 1ps ($\tau\sim$ 260 fs) a negative band peaking at 1.67eV forms along with the red shift of the PB, that falls outside our experimental range. Such a behavior has been well documented in semiconductors as a result of self-normalization of the exciton energy– i.e. blue shift of the exciton absorption – due to exciton-exciton and exciton-carrier interaction[24–28]. Thus, the negative band is the result of a modulation (in the following we indicate it as MA*) and can be considered as a fingerprint for exciton population[24,26]. As previously asserted, large crystals show a clear excitonic transition at the absorption edge that gains strength upon cooling [7,12,29]. Even considering the lowest exciton binding energy reported so far in literature (i.e. 5meV[14,16, 30]), one can expect a decent exciton population at 170K, at the photoexcitation densities used (a simple guideline to estimate exciton population fraction depending on the exciton binding energy value, temperature and excitation density is presented in Figure S8). Accordingly, at 170K the formation of MA* is indicative of exciton formation upon carrier thermalization. We estimate that the carrier coalescence into the bound excitonic state occurs within 1 ps (see dynamics in Figure 1f), consistent with the similar phonon

assisted phenomenon that occur in the band relaxation. Note that in 2D hybrid perovskites the formation of MA* has also been reported, although slower[24,28].

In this specific morphology, the exciton population appears only upon temperature reduction, implying that the exciton binding energy is insufficient to stabilize the exciton population at RT. To broaden the perspective of our observation we fabricated "cuboids-like" films of $MAPbI_3$[20], with controlled crystal dimension of either < 200 nm or ~ 1 μm from visual inspection of SEM images in Figure 2a and 2b respectively (see Figure S1 in SI for the XRD analysis). The UV-vis absorption spectra at RT are shown in Figure S9 in the Supplementary Information. The TA spectrum of the film with < 200 nm crystal size (indicated in the legend of Figure 2c as "small crystals") closely resembles the one obtained in the "meso phase" of the $MAPbI_3$ film at RT, showing that the thermalized carriers stay free at the band edge - see TA spectra at 1ps, after carrier thermalization, in Figure 2c and the entire spectral dynamics in Figure S10. No exciton feature is present. On the contrary, the sample made of ~1 μm large crystals exhibits, at RT, different spectral features and dynamics. The TA spectrum forming in 1ps upon photoexcitation above band-gap resembles the one of the capping layer at 170K (Figure 2c). In particular we highlight the presence of the MA* band even at RT, with a formation time of about 270 fs (see inset in Figure 2d). Note that this sample keeps the same TA spectral features even at 77K, where a clear stable excitonic state is also present at the band edge (see UV-Vis spectra in Figure S6 in the SI), albeit shifted to higher energies (about 95 meV, see TA spectrum in Figure S7 in the SI) as consequence of a phase transition. In Figure 2c the red-shifted TA spectrum taken at 77K is reported (dashed line) for easier comparison. This provides additional support to

our assignment of the TA spectra, and the correct prediction of a bleaching band just outside the experimental range. In Figure 2d we show the details of the spectral evolution of the sample with large crystals. Importantly, at longer time delays (>10 ps) the MA* band reduces and the PB shifts to higher energies, towards the free carrier bleach. This dynamic reflects the decay of the excitonic population that appears to be shorter lived with respect to the free carrier population, as further confirmed by the TA spectra in the ns time regime (see Figure S11 in the SI).

We have shown so far that different morphologies of $MAPbI_3$ thin films – with average crystal size varying from tens to hundreds of nm may *i)* support only the free carrier population, even at low temperature; *ii)* support an excitonic population upon temperature reduction; *iii)* sustain the formation of a fraction of short living excitons at room temperature. Since the photo-excitation density used in the above three cases is the same, this clearly indicates that the electron-hole interaction is modified by the degree of polycrystallinity in the film (please refer to Figure S8 for a simple visualization of the variation of exciton population fraction as a function of exciton binding energy at a given photoexcitation density). Thus, the exciton binding energy is not uniquely determined by the chemical composition of the polycrystalline material but it can be tuned in a range between a few to tens of meV[14–16].

To further generalize our observations we also consider thin films of $MAPbBr_3$. The halogen substitution induces a lowering of the valence band of the semiconductor and a blue shift of the optical gap, making the material appealing for a variety of applications such as high Voc solar cells[31,32], water splitting and light emitting devices[3,6]. Seminal studies have suggested larger exciton binding energy for $MAPbBr_3$ with respect to

$MAPbI_3$ [33]. However, the optical spectra reported by some of the recent works[32,34,35] do not show any strong excitonic feature at RT. To verify the role of morphology also in this system we prepared $MAPbBr_3$ thin films with average crystal dimensions much smaller than 100 nm by growing them in an Al_2O_3 mesoporous scaffold and ~1 μm (see SEM images in Figure S12 of SI). Figure 3a and Figure 3b show the UV-vis spectra of such samples while Figure 3c and Figure 3d show the photo-induced TA spectra when exciting above band-gap at RT. Small crystals do not show any excitonic feature at the on-set of the UV-vis absorption spectrum, at RT. In perfect agreement, the TA spectrum resembles very much, in shape and dynamics, that from meso $MAPbI_3$, pointing to a free carrier picture (refer to Figures S3 and S4 and the discussion in the SI). In contrast, large crystals show a sharp excitonic feature at the onset of the absorption spectrum (Figure 3b). In agreement, the TA spectra (Figure 3d) of the large $MAPbBr_3$ crystals show the formation of a PB band at 2.34 eV that matches with the excitonic transition, together with the appearance of the modulation feature, MA*, at 2.43 eV in the first ps (a comparison of the 1ps spectra from the small and the large crystal is reported in the inset of Figure 3d). This behavior indicates the formation of an exciton population upon carrier thermalization which eventually recombines in hundreds of ps. The latter is clearly demonstrated by the fact that beyond 1ps the spectra lose their intensity but do not change their spectral shape (see also dynamics in Figure S13 of the SI).

These results show that also for $MAPbBr_3$ it is not possible to asses a unique value for the exciton binding energy, which will depend on the thin film morphology. Thus, optoelectronic devices made of large $MAPbBr_3$ crystals, with a stable excitonic

population at RT, will work in a different manner with respect to those made of thin films with a higher degree of polycrystallinity.

The effect of the degree of polycrystallinity on the exciton binding energy can be rationalized by considering the role of disorder in such hybrid systems, with particular emphasis on the orientational order of the organic cation within the material. Large perovskite crystals (~1 μm in size) show a cooperative ordered phase of the organic cations which affects their rotational degrees of freedom[9,36]. This is not intrinsically related to the size of the crystal, but to the "quality" of the crystallization process. We have shown recently that the crystallization process does affect the optoelectronic properties through the modulation of the lattice strain[8,13]. Raman analysis [9,29] on the meso-phase of $MAPbI_3$ (see Figure S14 in the SI) suggests a more distorted structural arrangement, thus dipoles in the small crystals might be more randomly oriented within the inorganic cage. Of course, this can be induced by different factors, e.g. the crystallization procedure, the presence of dangling bonds on the surface, or the influence of external agents.

The organic cation has a permanent dipole moment, generating an electrostatic potential. If free to rotate, the dipoles will respond in a dielectric manner. This increases the low frequency (hundreds of GHz) dielectric constant up to 35 [37,38] in $MAPbI_3$. The Mott-Wannier exciton binding energy can be written as $E_b = \frac{m^* e^4}{\hbar^2 \varepsilon^2}$. If we take the optical frequency dielectric constant (ε ~ 5) this value is 45 meV, with an effective exciton Bohr radius of 4 nm. The binding energy is in very good agreement with the experimental value of ~50 meV [12]. However, this model is valid only if the Coulomb interaction

between the electron and hole is strong enough (and thus the kinetic energy of the small exciton high enough) that the slower lattice dielectric response does not screen the interaction. If the exciton is less strongly bound, we must consider also the low frequency component of the dielectric constant arising from the lattice contributions. This would result in the exciton sampling a higher dielectric constant, thus decreasing its binding energy (to 2 meV) and increasing the size to 19 nm, eventually dissociating it. In order to see how the different screening regimes are linked to the crystallization process we consider the microscopic effect of disorder and temperature by sampling the electrostatic potential resulting from simulating mono-crystalline and polycrystalline films. We describe the changes in electrostatic potential upon moving from a large grain to microcrystalline structure by extending a Monte Carlo procedure based upon a model Hamiltonian parameterized for $MAPbI_3$ [39]. The grain boundaries are induced by incorporating inactive lattice sites ("point defects") in the simulation (at densities of 6% and 10%), which enforces polycrystallinity within the simulation domains. The standard deviation in the electrostatic potential is plotted as a function of temperature and defect density (degree of polycrystallinity) in Figure 4 (top panel), while representative domain structures, and associated electrostatic potentials, are shown in Figure 4a-c (bottom panels).

For the mono-crystalline system, the standard deviation in the electrostatic potential drops to zero with decreasing temperature. All the rotational disorder of the organic cations is quenched leading to complete order and formation of fully twinned domains. Disorder grows with temperature as would be expected from statistical mechanics, generating increasing electrostatic potential variance. We note that this is in full

agreement with a recent work published by R. Nicholas and co-workers, which reports an increase in the exciton binding energy upon reduction of temperature[16]. At room temperature, the electrostatic potential is fairly disordered, with a standard deviation of 163 meV, and the degree of polycrystallinity matters less at the level of defect density considered as all samples are thermally disordered. At lower temperatures however, the variation in electrostatic potential is proportional to the degree of polycrystallinity and does not disappear at 0K for the polycrystalline films (explicit tetragonal-orthorhombic phase transitions are not treated by the model). The largest variation in electrostatic potential occurs at grain boundaries, where the dipole twinning is disrupted (see Figure 4a-c bottom panels, dipoles alignment are represented in different morphologies and temperatures). These simulations confirm an interesting trend, that the variance of the electrostatic potential (i.e. local screening) can be controlled by the local order within the crystal. With larger, less defective, crystals the variance is minimized. Thus, electron-hole separation due to electrostatic disorder should be significant in small crystals (countering the Coulomb attraction between electrons and holes) but weaker in large crystals (allowing for Wannier exciton formation).

A single crystal sample should represent the ultimate case study for our model. However, as mentioned earlier, discrepancies can be found in literature with regards to the optical properties of such a sample[17,18]. Indeed we have observed that a single crystal can show energetic dishomogeneity within surface and bulk phases with respect to the optical gap, following the same trend as the small and large crystallites (see Figure S15 in the SI). This can be understood from the presence of defects and fluctuations at the crystal termination. The surface of the single crystal is an extended

defect and it should be considered as comparable to the sample made of small crystallites. Due to the high absorbance of the single crystal, the absorption spectra presented in literature have been measured through reflectivity[17,18], which is more sensitive to the surface rather than the bulk of the semiconductor. Thus, according to our model, we do not expect to see excitonic features. On the other hand, we have noticed that the EQE spectra (which may be more sensitive to the bulk properties of the semiconductor) of solar cells embodying single crystal of $MAPbI_3$ shows a defined exciton like peak at the band edge in contrast to polycrystalline thin-film based devices[18]. This observation suggests the strengthening of an excitonic transition, at room temperature, in the bulk of the single crystal as we predict.

Thus we conclude that the sensitivity of the molecular order to the crystal quality, defects, as well as induced strain and device history, implies that there is considerable scope in the material processing to tune the nature and the dynamics of the photophysical mechanisms characterizing each sample. Control of the dynamic polarization effect, which can provide both free carrier and excitonic regimes for a single material composition, may open up a plethora of novel optoelectronic applications.

Experimental Methods:

Synthesis of the Precursor solutions:

Methylammonium iodide salt: The precursor solution of perovskite was prepared following the well-established method reported in literature[1].Methylamine solution (33% wt. in absolute ethanol, Sigma-Aldrich) was reacted with hydroiodic acid (57% wt. in

water, Sigma-Aldrich), with excess methylamine in ethanol at 0°C. Crystallization of CH_3NH_3I was achieved using a rotary evaporator; a white colored powder was formed, indicating successful crystallization. The salt was washed twice in diethyl ether to remove impurities.

Methylammonium bromide salt. The solution was prepared as reported elsewhere[6].The solution was prepared by adding methylamine solution (33% wt. in absolute ethanol, *Sigma-Aldrich*) and hydrobromic acid (48% wt. in water, Sigma-Aldrich) to 100 ml of absolute ethanol. The reaction mixture was stirred at 0°C. The solvent was removed by rotary evaporation. The obtained white crystals were washed with anhydrous diethyl ether and recrystallized in ethanol. The perovskite precursor solution was prepared by mixing CH_3NH_3Br and $PbBr_2$ in a 1:1 molar ratio in anhydrous N,N-dimethylformamide to give concentrations of 20% and 5% wt.

Preparation of samples for spectroscopy:

All the samples were prepared in a controlled nitrogen atmosphere either on glass microscope slides or on mesoporous Al_2O_3.

Mesoporous Al_2O_3: a commercial alumina nanoparticles dispersion (20% wt. in IPA, nanoparticles average size around 50 nm, *Sigma-Aldrich*) was spin-coated at 2000 rpm to form a ~3 μm thick mesoporous layer. These were then dried at 150°C for 30 minutes in air and 10 minutes under inert atmosphere.

$CH_3NH_3PbI_3$ deposition method on mesoporous Al_2O_3: A hot (70°C) solution of PbI2 in DMF (0.5M) was spin coated at 2000 rpm for 60 seconds and subsequently annealed at 70°C for 30 minutes. After letting it cool down to room temperature, the substrate was

dipped at room temperature in a CH_3NH_3I solution (0.063 M) in anhydrous IPA for 2 minutes. Samples are finally rinsed in anhydrous IPA to remove the excess of unreacted CH_3NH_3I .

Glass: the substrates were cleaned (two cycles of water, acetone and IPA in an ultrasonic bath for 10 minutes each) followed by an oxygen plasma treatment for 10 minutes.

$CH_3NH_3PbI_3$ deposition method on glass: A hot (70°C) solution of PbI_2 in DMF (1M) was spin coated at 2000 rpm for 60 sec in order to obtain a 300 nm thick layer. A subsequent annealing at 70°C for 30 min was required to obtain the PbI_2 thin film. After letting it cool down to room temperature, the substrate was dipped in a CH_3NH_3I solution in anhydrous IPA for 2 minutes. To obtain samples with different crystal sizes, the concentration and temperature of CH_3NH_3I was varied. To obtain films with ~100 nm crystals (Figure 2a), the concentration was set at 0.063 M, and the dipping was performed at room temperature, while the concentration was reduced to 0.045 M and the bath was warmed up to 70°C to obtain crystals above 1μm large (Figure 2b). Samples are finally rinsed in anhydrous IPA to remove the excess of unreacted CH_3NH_3I.

$CH_3NH_3PbBr_3$ one step-deposition method: CH_3NH_3Br and $PbBr_2$ were both dissolved in DMF (concentration of 20% wt. for the deposition on glass substrate and 10%wt. for deposition in the mesoporous alumina scaffold). The solution was spin coated at 3000 rpm for 60 seconds. A subsequent annealing at 100°C for 15 min is required to obtain the perovskite thin film.

Scanning Electron Microscopy

High Resolution Scanning Electron Microscopy (HRSEM) was used for Figures 1a and 1d. The samples were sticked on aluminum stubs with ultra smooth double-sided adhesive tape, made of conductive carbon, specific for UHV systems and then coated with a 15 nm layer of conductive amorphous carbon. HRSEM observation was carried out using a JEOL JSM 7500FA scanning electron microscope, equipped with a cold field emission gun (single crystal tungsten <310> emitter, ultimate resolution of 1 nm) and operating at 10 kV.

The SEM images shown in Figures 2 have been collected by using an high vacuum tungsten filament commercial Jeol 6010-LV, with a working bias of 20 kV.

Ultraviolet–visible absorption

Absorption spectra have been recorded using a UV-VIS-NIR spectrophotometer (PerkinElmer Lambda 1050 model) with a spectral range from 200 nm to 2000 nm, with a resolution of about 1 nm.

Femtosecond transient absorption set-up:

In a typical pump-probe experiment, the system under study is photoexcited by a short pump pulse (~120 fs) and its subsequent dynamical evolution is detected by measuring the transmission changes ΔT of a delayed probe pulse as a function of pump-probe delay and probe wavelength . The signal is given by the differential transmission ΔT/T = [(Tpump on-Tpump off)/Tpump off]. The system is driven by a mode-locked Ti:Sapphire oscillator (Coherent Micra-18) operating at 80 MHz was used as a fundamental

broadband source. This provided pulses with durations of ~20 fs and a central wavelength of 800 nm. A grating based pulse stretcher (Coherent 9040) was used to temporally expand the pulses before amplification in a 250 kHz actively Q-switched Ti:Sapphire based regenerative amplifier (Coherent RegA 9000). The amplified pulses were subsequently temporally compressed in a grating based compressor (Coherent 9040), resulting in pulses with temporal widths of ~35 fs and energies of ~6 μJ. A thin beam splitter is used to split the amplified output into pump and probe beams. The pump beam is input into a two-pass BBO-based collinear OPA (Coherent 9450), allowing spectral conversion to any desired wavelength in the 480-750 nm wavelength range with resulting temporal broadening to ~120 fs. The probe beam was used for super-continuum generation within a sapphire plate, leading to probe pulses with significant continuous spectral content from 480-780 nm and temporal widths of ~100 fs. Both pump and probe pulses were focused and spatially overlapped in the sample space, with the temporal delay between them given by an optical retro-reflective delay line located on the pump arm of the system. Great care was taken to ensure the spot size of the probe beam was significantly smaller than that of the pump beam. The resulting probe signal typically measured in transmission is coupled into an Acton SP2300i imaging spectrograph and the dispersed signal was measured by a custom (Stresing) silicon based CCD linear array. The minimum detectable signal is $\Delta T/T \sim 10^{-5}$. The pump beam energy density used in the experiment is kept deliberately low (pump fluence less than 1 $\mu J/cm^2$, which results in excitation densities in the order of 10^{17} cm^{-3}). All the measurements were taken with the samples in a vacuum chamber to prevent any influence from oxygen or sample degradation. The temperature-dependent

experiments were carried out using a continuous flow static exchange gas cryostat (*Oxford Instruments*).The cryostat consist of three chambers, one inside the other. The sample is housed inside the internal chamber filled with gaseous nitrogen. The cryogenic liquid (N_2) is fluxed inside the second chamber allowing temperature control of the N_2 atmosphere of the sample chamber. Eventually a third chamber is evacuated (~ 10^{-5} - 10^{-6} mbar) in order to assure thermal isolation from the external ambient. A sensor close to the sample has been mounted in order to accurately monitor the sample temperature.

Theoretical Simulations

The Starrynight (molecular ferroelectric simulation) code[39] was adapted to model defective domains. Simulations were carried out in two dimensions with a 25 meV interaction between near-neighbour dipoles, no cage-strain term, a 3 unit-cell cut-off for dipole interactions and periodic boundary conditions on a two dimensional 250×250 grid. Strain (ordering) terms would be required to fully describe the tetragonal-orthorhombic phase transition and are expected to increase the order-disorder transition temperature of a phase, and so the effective temperature reported in Figure 4 may be considerably higher. The initial dipole orientation was random. 10^5 Monte-Carlo moves were attempted per site, with a Metropolis algorithm. The electrostatic potential variation was calculated from the sampled dipole orientation at equilibrium with a 10 unit-cell cut-off.

References:

1. Zhou, H. *et al.* Interface engineering of highly efficient perovskite solar cells. *Science* **345,** 542–546 (2014).

2. Grätzel, M. The light and shade of perovskite solar cells. *Nat. Mater.* **13,** 838–842 (2014).

3. Xing, G., Mathews, N., Lim, S. & Yantara, N. Low-temperature solution-processed wavelength-tunable perovskites for lasing. *Nat. Mater.* **13,** 476–480 (2014).

4. Deschler, F. *et al.* High Photoluminescence Efficiency and Optically Pumped Lasing in Solution-Processed Mixed Halide Perovskite Semiconductors. *J. Phys. Chem. Lett.* **5,** 1421–1426 (2014).

5. Zhu, H. *et al.* Lead halide perovskite nanowire lasers with low lasing thresholds and high quality factors. *Nat. Mater.* **14,** 636-642 (2015).

6. Tan, Z.-K. *et al.* Bright light-emitting diodes based on organometal halide perovskite. *Nat. Nanotechnol.* **9,** 687 – 692 (2014).

7. Ball, J. M., Lee, M. M., Hey, A. & Snaith, H. J. Low-temperature processed meso-superstructured to thin-film perovskite solar cells. *Energy Environ. Sci.* **6,** 1739 (2013).

8. De Bastiani, M., D'Innocenzo, V., Stranks, S. D., Snaith, H. J. & Petrozza, A. Role of the crystallization substrate on the photoluminescence properties of organo-lead mixed halides perovskites. *APL Mater.* **2,** 081509 (2014).

9. Grancini, G. *et al.* The Impact of the Crystallization Processes on the Structural and Optical Properties of Hybrid Perovskite Films for Photovoltaics. *J. Phys. Chem. Lett.* **5,** 3836–3842 (2014).

10. Marchioro, A. *et al.* Unravelling the mechanism of photoinduced charge transfer processes in lead iodide perovskite solar cells. *Nat. Photonics* **8,** 250–255 (2014).

11. Manser, J. S. & Kamat, P. V. Band filling with free charge carriers in organometal halide perovskites. *Nat. Photonics* **8,** 737 – 743 (2014).

12. D'Innocenzo, V. *et al.* Excitons versus free charges in organo-lead tri-halide perovskites. *Nat. Commun.* **5,** 3486 (2014).

13. D'Innocenzo, V., Srimath Kandada, A. R., De Bastiani, M., Gandini, M. & Petrozza, A. Tuning the light emission properties by band gap engineering in hybrid lead-halide perovskite. *J. Am. Chem. Soc.* **136,** 17730–17733 (2014).

14. Lin, Q., Armin, A., Nagiri, R. C. R., Burn, P. L. & Meredith, P. Electro-optics of perovskite solar cells. *Nat. Photonics* (2014). doi:10.1038/nphoton.2014.284

15. Saba, M. *et al.* Correlated electron-hole plasma in organometal perovskites. *Nat. Commun.* **5,** 5049 (2014).

16. Miyata, A. *et al.* Direct Measurement of the Exciton Binding Energy and Effective Masses for Charge carriers in an Organic-Inorganic Tri-halide Perovskite. *Nat. Phys.* **11**, 582-587 (2015).

17. Shi, D. *et al.* Low trap-state density and long carrier diffusion in organolead trihalide perovskite single crystals. *Science* **347,** 519–522 (2015).

18. Dong, Q. *et al.* Electron-hole diffusion lengths > 175 μm in solution-grown CH3NH3PbI3 single crystals. *Science* **347,** 967 – 970 (2015).

19. Nie, W. *et al.* High-efficiency solution-processed perovskite solar cells with millimeter-scale grains. *Science* **347,** 522–525 (2015).

20. Im, J.-H., Jang, I.-H., Pellet, N., Grätzel, M. & Park, N.-G. Growth of CH3NH3PbI3 cuboids with controlled size for high-efficiency perovskite solar cells. *Nat. Nanotechnol.* **9,** 927–932 (2014).

21. Xing, G. *et al.* Long-range balanced electron- and hole-transport lengths in organic-inorganic CH3NH3PbI3. *Science* **342,** 344–7 (2013).

22. Varshni, Y. P. Temperature dependence of the energy gap in semiconductors. *Physica* **34,** 149–154 (1967).

23. Onoda-Yamamuro, N., Matsuo, T. & Suga, H. Calorimetric and IR spectroscopic studies of phase transitions in methylammonium trihalogenoplumbates (II)†. *J. Phys. Chem. Solids* **51,** 1383–1395 (1990).

24. Shimizu, M., Fujisawa, J.-I. & Ishi-Hayase, J. Influence of dielectric confinement on excitonic nonlinearity in inorganic-organic layered semiconductors. *Phys. Rev. B* **71,** 205306 (2005).

25. Hulin, D. *et al.* Well-size dependence of exciton blue shift in GaAs multiple-quantum-well structures. *Phys. Rev. B* **33,** 4389–4391 (1986).

26. Peyghambarian, N. *et al.* Blue shift of the exciton resonance due to exciton-exciton interactions in a multiple-quantum-well structure. *Phys. Rev. Lett.* **53,** 2433–2436 (1984).

27. Schmitt-Rink, S., Chemla, D. & Miller, D. Theory of transient excitonic optical nonlinearities in semiconductor quantum-well structures. *Phys. Rev. B* **32,** 6601–6609 (1985).

28. Wu, X., Trinh, M. T. & Zhu, X. Excitonic Many-Body Interactions in Two-Dimensional Lead Iodide Perovskite Quantum Wells. *J. Phys. Chem. C* (2015). doi:10.1021/acs.jpcc.5b00148

29. Quarti, C., Grancini, G. & Mosconi, E. The Raman Spectrum of the CH3NH3PbI3 Hybrid Perovskite: Interplay of Theory and Experiment. *J. Phys. Chem. Lett.* **5,** 279–284 (2014).

30. Even, J. *et al.* Solid-State Physics Perspective on Hybrid Perovskite Semiconductors. *J. Phys. Chem. C* **119**, 10161-10177 (2015).

31. Heo, J. H., Song, D. H. & Im, S. H. Planar CH 3 NH 3 PbBr 3 Hybrid Solar Cells with 10.4% Power Conversion Efficiency, Fabricated by Controlled Crystallization in the Spin-Coating Process. *Adv. Mater.* **26,** 8179–8183 (2014).

32. Edri, E., Kirmayer, S., Cahen, D. & Hodes, G. High Open-Circuit Voltage Solar Cells Based on Organic–Inorganic Lead Bromide Perovskite. *J. Phys. Chem. Lett.* **4,** 897–902 (2013).

33. Tanaka, K. *et al.* Comparative study on the excitons in lead-halide-based perovskite-type crystals CH3NH3PbBr3 CH3NH3PbI3. *Solid State Commun.* **127,** 619–623 (2003).

34. Hoke, E. T. *et al.* Reversible photo-induced trap formation in mixed-halide hybrid perovskites for photovoltaics. *Chem. Sci.* **6,** 613–617 (2014).

35. Sadhanala, A. & Deschler, F. Preparation of Single-Phase Films of CH3NH3Pb (I1–x Br x) 3 with Sharp Optical Band Edges. *J. Phys. Chem. Lett.* **5,** 2501–2505 (2014).

36. Mosconi, E., Quarti, C., Ivanovska, T., Ruani, G. & De Angelis, F. Structural and electronic properties of organo-halide lead perovskites: a combined IR-spectroscopy and ab initio molecular dynamics investigation. *Phys. Chem. Chem. Phys.* **16,** 16137–44 (2014).

37. Wasylishen, R., Knop, O. & Macdonald, J. Cation rotation in methylammonium lead halides. *Solid State Commun.* **56,** 581–582 (1985).

38. Poglitsch, A. & Weber, D. Dynamic disorder in methylammoniumtrihalogenoplumbates (II) observed by millimeter-wave spectroscopy. *J. Chem. Phys.* **87,** 6373 (1987).

39. Frost, J. M., Butler, K. T. & Walsh, A. Molecular ferroelectric contributions to anomalous hysteresis in hybrid perovskite solar cells. *APL Mater.* **2,** 081506 (2014).

40. The pump-probe signal is due to the photo-excited volume, while the unexcited regions (however large) do not contribute. Transmission of the probe through the unexcited volume of the sample is cancelled out in the transmission difference signal.

Acknowledgments:

The research leading to these results has received funding from the European Union Seventh Framework Programme [FP7/2007-2013] under grant agreement n° 604032 of the MESO project. JMF is funded by the EPSRC (EP/K016288/ and EP/M009580/1), while AW is supported by the European Research Council (Project No. 277757). The authors thank Stefanie Neutzner for help with fs-TA experiments and Weidong Xu for help in sample preparation. The authors thank Dr. Eric T. Hoke, Emma R. Dohner and Prof. Hemamala Karunadasa for useful discussion and for providing the single crystal. The authors thank Prof. Liberato Manna for useful discussion and kind access to the XRD facility.

Author contributions:

GG, ARSK and AJB performed the Transient Absorption Measurements; MG and MDB prepared the samples and characterized them by SEM; SM performed XRD and SEM characterization. GG, ARSK, GL and AP analyzed the optical spectroscopy data; JMF and AW performed the multi-scale modelling and analyzed the results; the manuscript was written through contributions of all authors; AP supervised the project.

Figure Captions

Figure 1| Temperature-dependent transient absorption spectra of $MAPbI_3$ meso phase and capping layer. SEM images of (a) the “meso-phase” and of (b), the capping

layer of the 3μm-thick $MAPbI_3$ sample. Note that (a) is showing a zoom-in of figure (b). (c) Temperature dependence of the TA spectra at 1ps pump-probe delay of the meso phase; (d), Temperature dependence of the TA spectra at 1ps pump-probe delay of the "capping layer". (e), TA spectral evolution between 200fs and 1ns at 170 K of the capping layer. (f) dynamics probed at 1.72 eV (MA* band) of the capping layer at 170K compared to the dynamics probed at 1.64eV (PB band) of the same sample at RT. For all the TA measurements, the excitation wavelength is at 2.38eV with an excitation density of approximately 5×10^{17} cm^{-3}.

Figure 2| Photo-induced excited population of $MAPbI_3$ as a function of the crystal size. SEM images of perovskite films with average crystal dimension of: (a), $<$ 200 nm and (b), ~ 1μm. Scale bar: 2μm. (c), TA spectra, at room temperature, at 1 ps pump-probe delay of the two samples (red squares and blue circles, respectively) along with the TA spectrum (dashed line) of sample (b) taken at 77K, red shifted by 95meV. (d) TA spectra at different time delays at RT from the sample shown in (b). The inset shows the dynamics probed at 1.63 eV and 1.66 eV. For all the TA measurements, the excitation wavelength is at 2.38eV with an excitation density of approximately 5×10^{17} cm^{-3}.

Figure 3| Photo-induced excited population of $MAPbBr_3$ as a function of the crystal size. Uv-vis absorption spectra from MAPbBr3 films with average crystallite dimension (a) << 100 nm and (b), ~1μm. TA spectra at different time delays at RT from the sample with (c) small and (d) large crystallites (see SEM images in Figure S12 of

SI). In the inset of Figure 3d the comparison of the TA spectra at 1 ps of small and large $MAPbBr_3$ crystals. For all the TA measurements, the excitation wavelength is at 3.1 eV with an excitation density of approximately 1×10^{17} cm^{-3}

Figure 4| Multi-scale numerical simulations of dipole alignment in methylammonium lead iodide.

(Top) Standard deviation of electrostatic potential in Starrynight simulations of 250x250 interacting dipoles (150 x 150 nm crystallite), as a function of temperature. The standard variation in electrostatic for defect free perovskite crystals (blue) decays reduces to zero with a decrease in temperature. The 6% point defects (orange) and 10% point defect (red) trends show that there is non-vanishing disorder in the electrostatic potential, even at zero temperature. Below the figure we show small excerpts (25x25) of the simulation showing both dipole alignment (top) by pixel hue, and the resulting electrostatic potential (bottom). (a) Pure domains at zero Kelvin are highly ordered in a columnar antiferroelectric alignment leading to a smooth electrostatic potential, whereas defective crystals (b) at zero Kelvin contain electrostatic potential disorder as a result of frustrated alignment of the domains at the point defects. Room temperature domains (c) show that the thermal disorder at room temperature leads to a mostly paraelectric phase, with considerable electrostatic potential variance. (d) Schematic representation of electron-hole interaction driven by electrostatic potential fluctuations. In samples where there is considerable electrostatic potential variation, the exciton will not be stable.

570

Type of file: figure
Label: 1
Filename: figure_1.pdf

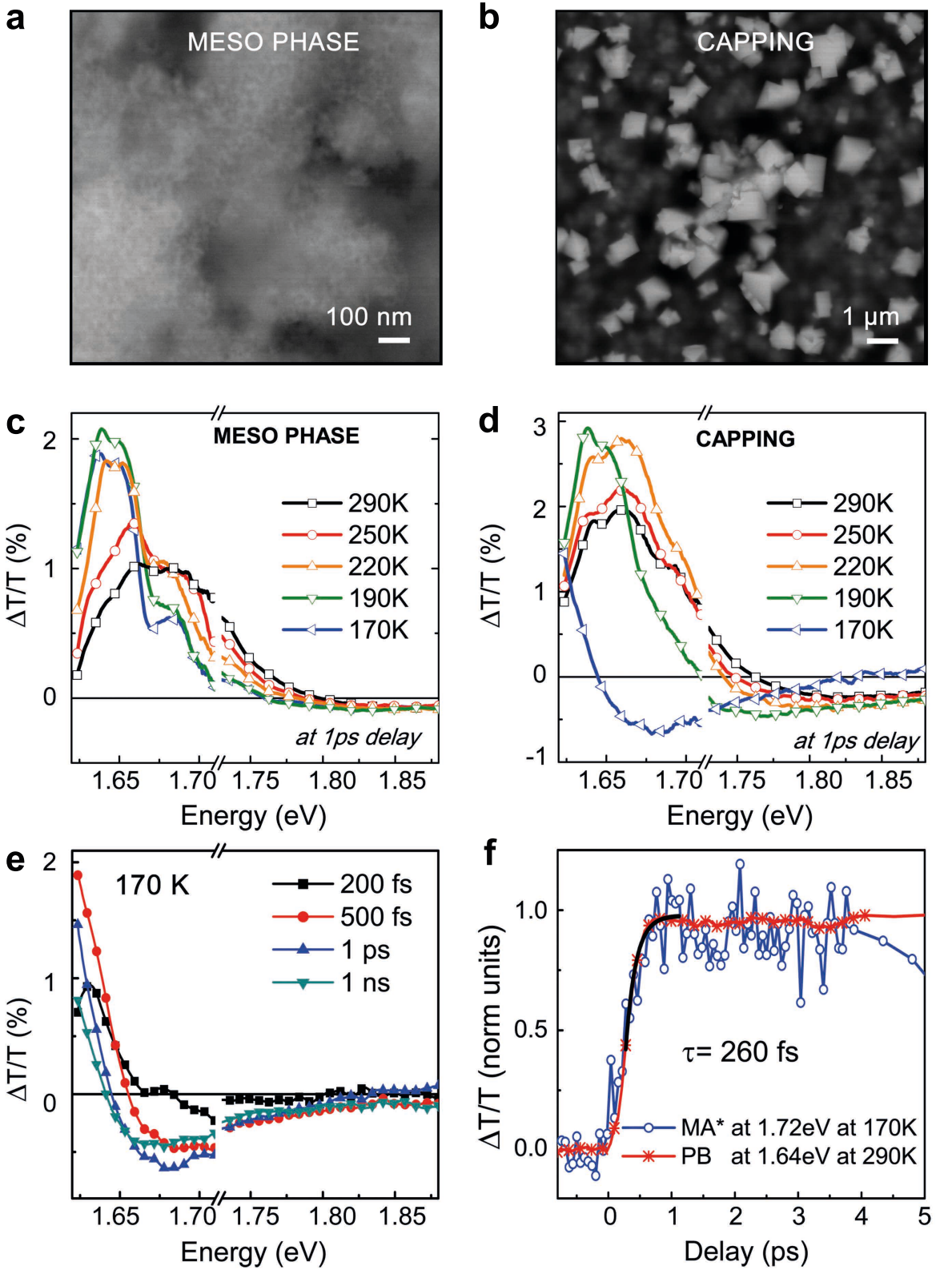
a
MESO PHASE
100 nm
b
CAPPING
1 μm
c
MESO PHASE
290K
250K
220K
190K
170K
at 1ps delay
ΔT/T (%)
Energy (eV)
d
CAPPING
290K
250K
220K
190K
170K
at 1ps delay
ΔT/T (%)
Energy (eV)
e
170 K
200 fs
500 fs
1 ps
1 ns
ΔT/T (%)
Energy (eV)
f
τ= 260 fs
MA* at 1.72eV at 170K
PB at 1.64eV at 290K
ΔT/T (norm units)
Delay (ps)

Type of file: figure
Label: 2
Filename: figure_2.pdf

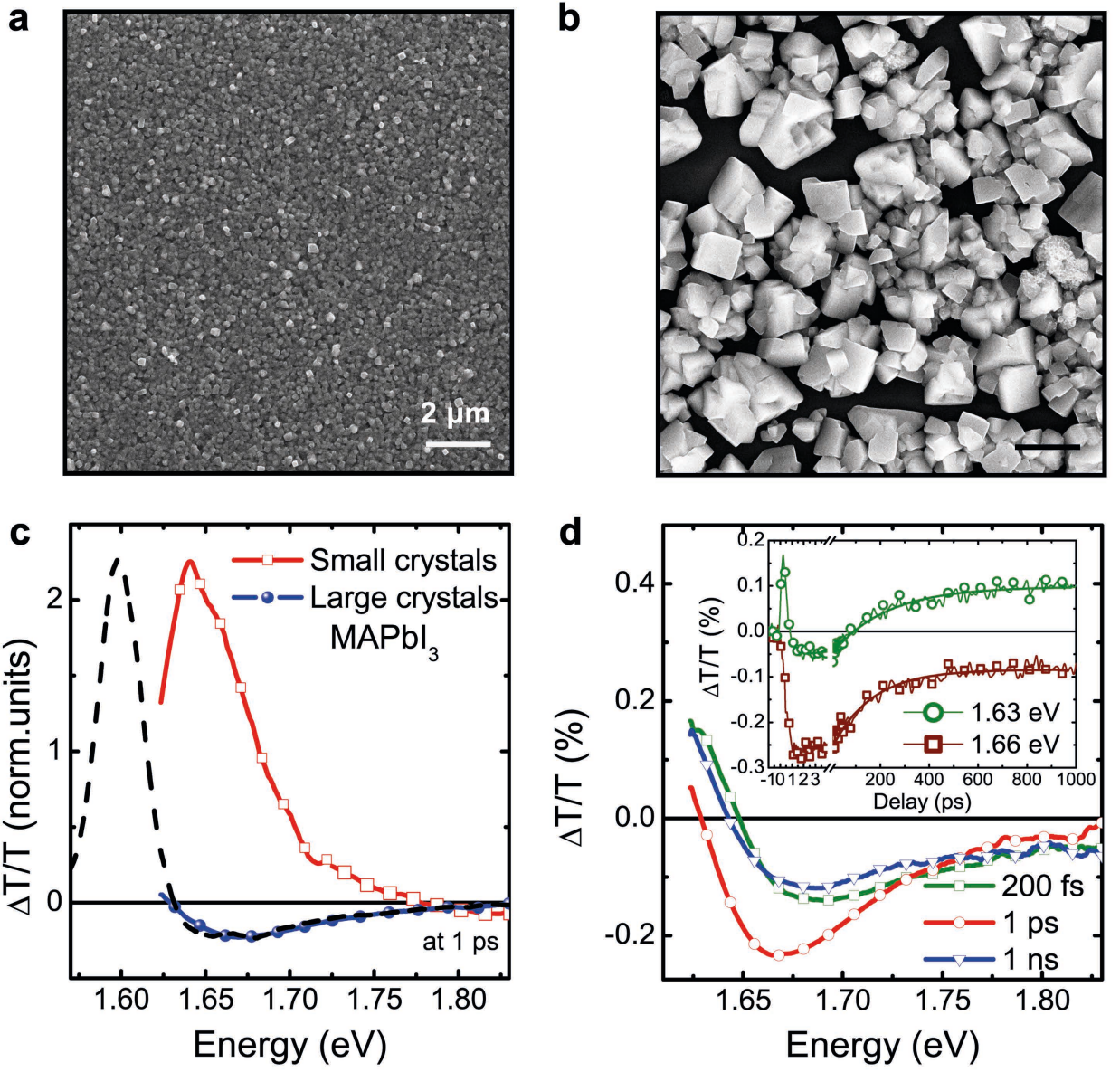
a
2 µm
b
c
Small crystals
Large crystals
MAPbI3
at 1 ps
ΔT/T (norm.units)
Energy (eV)
d
ΔT/T (%)
1.63 eV
1.66 eV
Delay (ps)
200 fs
1 ps
1 ns
Energy (eV)

Type of file: figure
Label: 3
Filename: figure_3.pdf

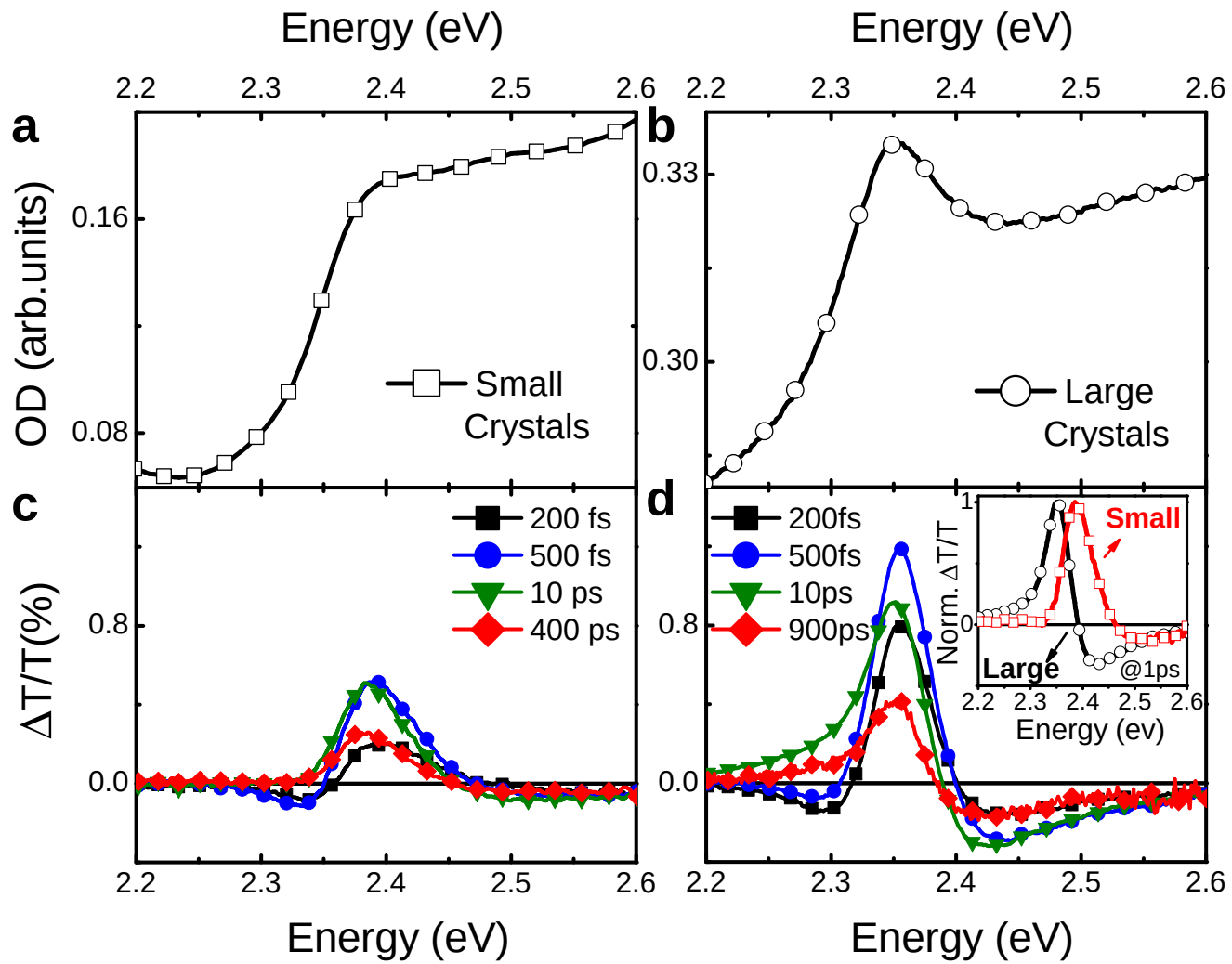
a
b
c
d
Energy (eV)
Energy (eV)
OD (arb.units)
0.16
0.08
0.33
0.30
Small
Crystals
Large
Crystals
ΔT/T(%)
0.8
0.0
200 fs
500 fs
10 ps
400 ps
200fs
500fs
10ps
900ps
Norm. ΔT/T
1
0
Small
Large
@1ps
Energy (ev)
2.2
2.3
2.4
2.5
2.6

Type of file: figure
Label: 4
Filename: figure_4.png

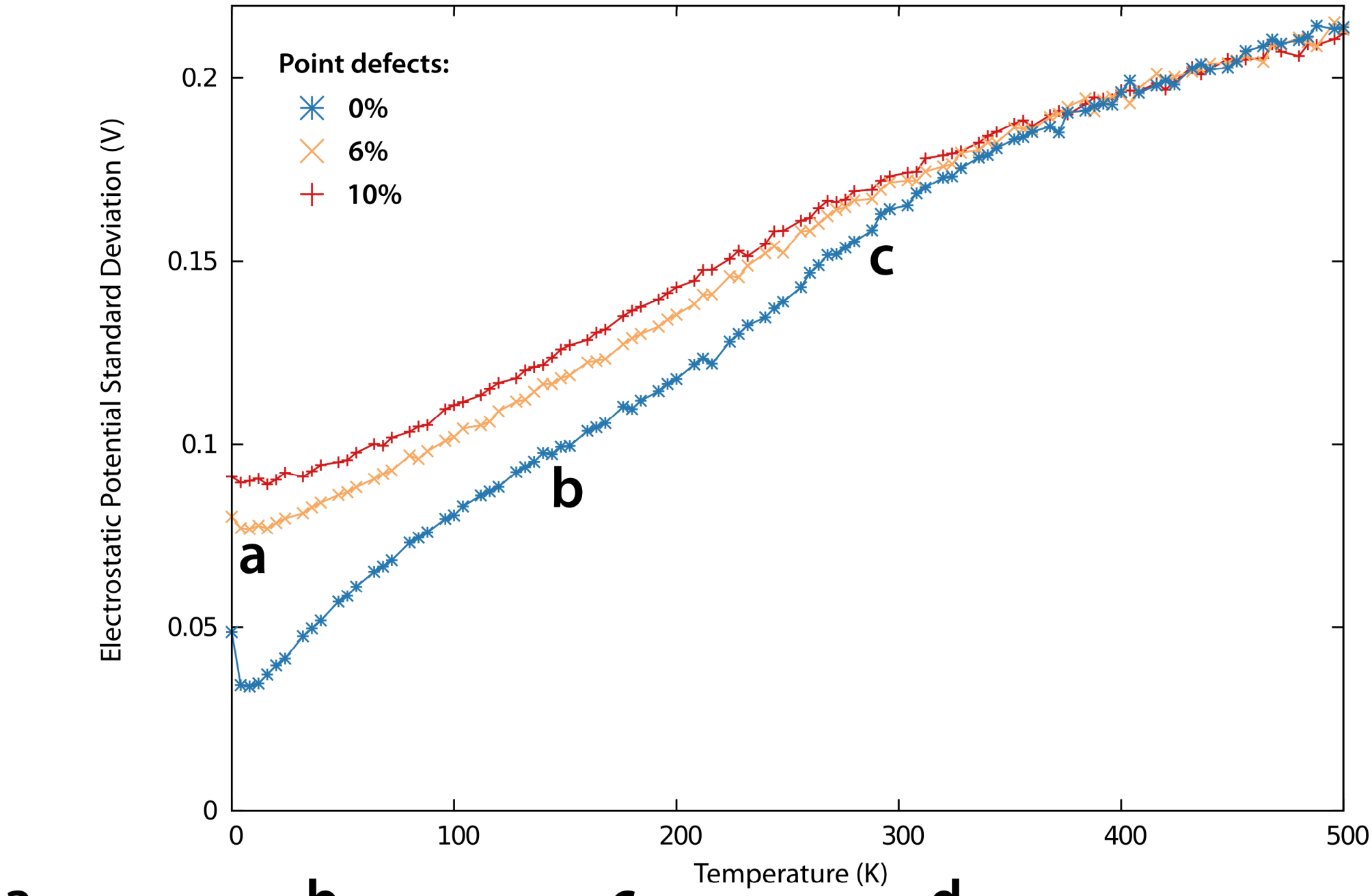
Point defects:
0%
6%
10%
Electrostatic Potential Standard Deviation (V)
0.2
0.15
0.1
0.05
0
0
100
200
300
400
500
Temperature (K)
a
b
c

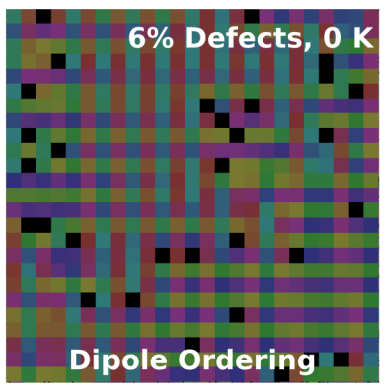
6% Defects, 0 K
Dipole Ordering

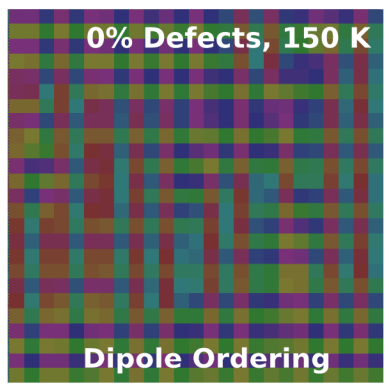
0% Defects, 150 K
Dipole Ordering

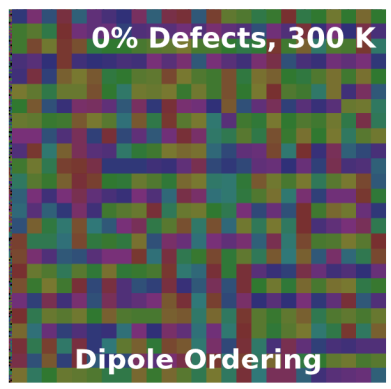
0% Defects, 300 K
Dipole Ordering

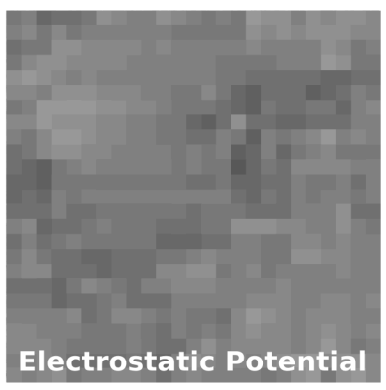
Electrostatic Potential

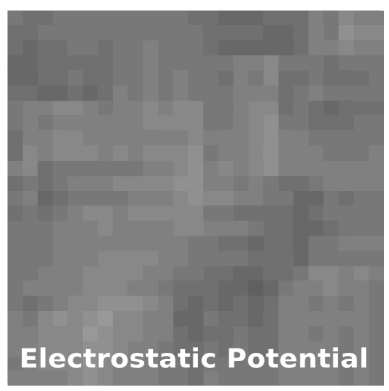
Electrostatic Potential

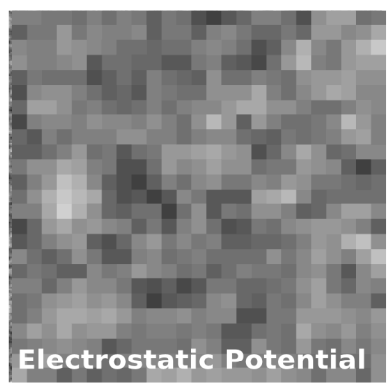
Electrostatic Potential

d

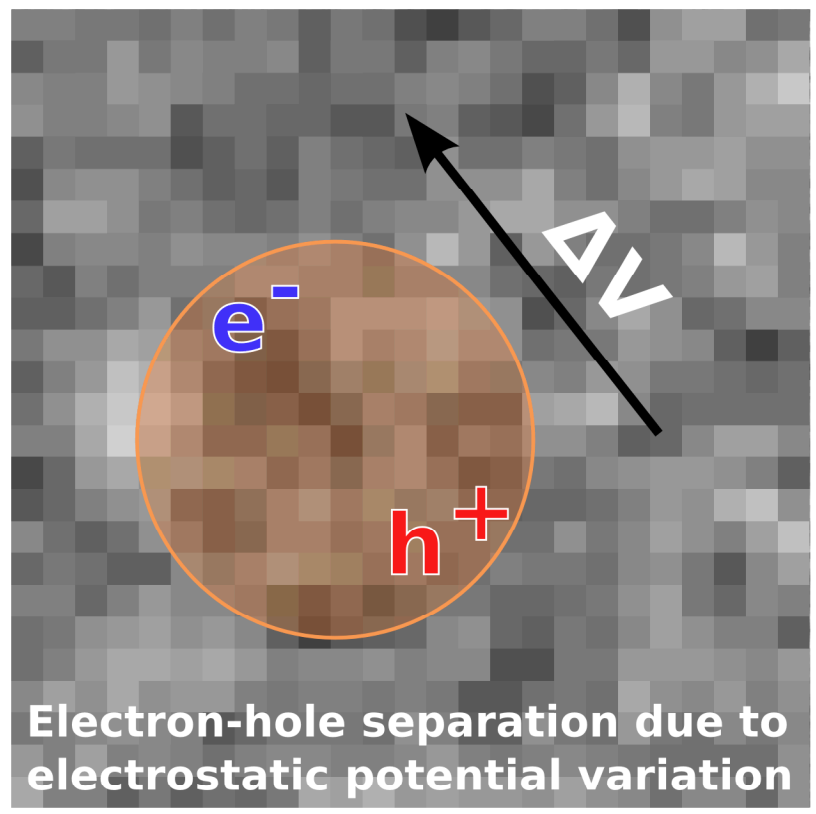
ΔV
e-
h+
Electron-hole separation due to
electrostatic potential variation

Europe PMC plus has received the file 'supp_info_1.pdf' as supplementary data. The file will not appear in this PDF Receipt, but it will be linked to the web version of your manuscript.